Journal of Materials Chemistry A

Unveiling the Photocatalytic Potential of Two-Dimensional Ferroelastic LuSX Monolayers for Efficient Water Splitting: A First-Principles Discovery

Journal:	*Journal of Materials Chemistry A*
Manuscript ID	TA-ART-11-2024-007900.R1
Article Type:	Paper
Date Submitted by the Author:	18-Jan-2025
Complete List of Authors:	Ma, Fengxian; Hebei Normal University Liu, Xiaoxia; Hebei Normal University Gao, Zhen; Hebei Normal University Chen, Zibo; Hebei Normal University, Physics Jiao, Yalong; Hebei Normal University, Physics Chen, Zhongfang; University of Puerto Rico, Department of Chemistry

Unveiling the Photocatalytic Potential of Two-Dimensional Ferroelastic LuSX Monolayers for Efficient Water Splitting: A First-Principles Discovery

Fengxian Ma,[a] Xiaoxia Liu,[a] Zhen Gao, [a] Zibo Chen, [a] Yalong Jiao,[a,*]
Zhongfang Chen[b,*]

[a] College of Physics, Hebei Key Laboratory of Photophysics Research and Application, Hebei Normal University, Shijiazhuang 050024, China.
[b] Department of Chemistry, University of Puerto Rico, Rio Piedras Campus, San Juan, PR 00931, USA.

*E-mail:
yalong.jiao@hebtu.edu.cn; zhongfang.chen1@upr.edu

Abstract

This study represents the first demonstration that two-dimensional (2D) ferroelastic (FE) materials can enhance photocatalytic applications. By comprehensive first-principles calculations, we identified the LuSX (X=Cl, Br, I) monolayers as novel FE photocatalysts for water splitting. These monolayers exhibit direct band gaps ranging from 3.67 eV to 4.09 eV, with favorable band edge alignments for photocatalytic water splitting across a range of pH values. The ferroelastic nature of LuSX enables tunable electronic properties through strain engineering, facilitating charge separation and enhancing photocatalytic efficiency. Our computations revealed their low FE switching barriers (as low as 0.12 eV per atom for LuSI) and high reversible FE strain, surpassing many known 2D materials. Furthermore, these LuSX monolayers exhibit strong UV-driven photocatalytic activity across all pH values without needing external strain. Under compressive strains, their ability to harvest a broader range of the solar spectrum is enhanced, significantly boosting their photocatalytic efficiency. These findings open up new avenues for using 2D ferroelastic materials in energy conversion applications, positioning LuSX monolayers as promising candidates for efficient, flexible photocatalysts.

Keywords

first-principles calculations, 2D materials, photocatalysts, ferroelastic materials

1. Introduction

Due to the increasing global population and the escalating consumption of fossil fuels, there is an unprecedented demand for alternative, renewable energy technologies that are both clean and economically viable. Among these, photocatalytic hydrogen production via solar water splitting emerges as a promising solution.[1, 2] In this process, semiconductors, when photoexcited by sunlight, generate charge carriers with sufficient energies to drive surface reactions. Two-dimensional (2D) materials have garnered significant attention as photocatalysts due to their unique advantages, such as large surface areas that facilitate reactions, short transport paths that reduce electron-hole pair recombination, and enhanced conductivity and mechanical properties.[3-6]

Though 2D semiconductors exhibit impressive photocatalytic properties, their activity can still be further enhanced through various strategies. These improvements often involve structural modifications and functional-system control.[7] Structural modifications can be achieved through methods such as defect engineering,[8] interface engineering,[9] and strain engineering.[10] On the other hand, functional-system control can be implemented by incorporating functional materials that either activate or accelerate photocatalytic performance, such as utilizing ferroelectric[11] and ferromagnetic materials,[12] or integrating with other semiconductors or metals.[13]

Ferroelastic (FE) materials, first recognized by Aizu in 1969,[14] exhibit a spontaneous strain and possess two or more stable orientational states without mechanical stress or an electric field.[15, 16] When mechanical stress is applied, these materials undergo a phase transition, resulting in a stress-induced spontaneous strain. Notably, ferroelastic materials are widely used

in applications leveraging shape memory and superelasticity. For example, Nitinol alloys can display these phenomena at room temperature, depending on their composition.

FE materials offer several potential advantages as photocatalysts: (1) Enhanced catalytic activity: The reversible phase transition in FE materials can induce atomic-level structural rearrangements, alternating surface morphology and exposing new active sites, thus improving catalytic activity by modifying reactants' adsorption/desorption behavior. (2) Potential for strain engineering: The reversible nature of ferroelasticity allows controlled strain to be introduced, optimizing the electronic and geometric properties of active sites for improved catalytic reactions. (3) Facile control of morphology: FE phase transitions create domains with varying orientations, facilitating the separation of photogenerated electrons and holes and reducing recombination rates, thereby enhancing photocatalytic efficiency. (4) Enhanced durability: FE materials are known for their remarkable resilience and resistance to mechanical deformation, making them ideal for catalytic applications under harsh reaction conditions.

Despite the numerous advantages of FE materials, their potential for photocatalytic water splitting remains largely unexplored. Given the unique properties of FE materials, such as strain-induced phase transitions and enhanced catalytic activity, it is imperative to investigate the potential of 2D FE materials for photocatalytic water splitting. Notably, very recently, Wang *et al.* predicted that a FE Y_2Se_2BrF monolayer exhibits photocatalytic properties.[5] However, the FE and photocatalytic properties were treated as separate phenomena, leaving the potential synergy between them—specifically how FE might enhance photocatalytic activity— unexamined. Unveiling this relationship could unlock new avenues for highly

efficient, durable photocatalysts, representing a breakthrough in sustainable energy technologies.

In this work, by means of first-principles calculations, we identified LuSX (X= Cl, Br, I) as viable 2D FE photocatalysts for overall water splitting. While 2D FE materials in binary systems have been extensively studied,[17-19] ternary structures have received comparatively less attention.[20] However, incorporating a third element into 2D FE materials offers greater chemical and structural diversity, enabling tunable electronic properties that are often unattainable in binary systems. These LuSX monolayers exhibit a spontaneous FE phase transition and crystallize in an orthorhombic FE phase with *Pmmn* symmetry. They display excellent ferroelasticity, characterized by low switching barriers and strong FE signals, making them appreciable for shape memory device applications. Importantly, these monolayers are semiconductors with band gaps ranging from 3.67 eV to 4.09 eV. By aligning their band-edge positions with the redox potentials of water, we confirmed their potential for water splitting. Moreover, the high carrier mobility of LuSBr along the Γ-X and Γ-Y lines can be directionally tuned by FE strain, offering a means to effectively modulate their photocatalytic performance.

2. Computational methods

Density functional theory (DFT) computations were performed using the plane-wave VASP code.[21] The projector-augmented-wave (PAW) potential was utilized to describe the interactions between the ionic cores and the valence electrons, [22] and the valence electron configuration for Lu is $4f^{14}\ 5s^2\ 5p^6\ 5d^1\ 6s^2$. Geometry optimizations were conducted with the generalized gradient approximation in the Perdew, Burke, and Ernzerhof form (GGA-PBE),[23] while the Heyd−Scuseria−Ernzerhof (HSE) functional was employed to estimate electronic

band gaps more accurately. Electronic wave functions were expanded using a plane-wave basis set with an energy cutoff of 500 eV.

To study 2D systems under periodic boundary conditions, a vacuum layer of at least 15 Å was applied to minimize artificial interactions between adjacent layers. Geometry optimizations utilized a Monkhorst−Pack k-point grid of 8 × 6 × 1, with all atoms fully relaxed until the residual force and energy converged to 0.01eV/ Å and 10^{-7} eV, respectively. Phonon dispersion analyses were carried out using the Phonopy code within the density functional perturbation theory (DFPT) framework.[24] The materials' thermal stabilities were evaluated by *ab initio* molecular dynamics (AIMD) simulations.

Reliable band alignments for photocatalytic water splitting were derived from HSE06 calculations. The vacuum potential was used as a reference to align the average electrostatic potential within the unit cell.

3. Results and Discussions

3.1. Structural properties and stability

Bulk LuSBr crystallizes in a three-dimensional (3D) layered structure with orthorhombic *Pmmn* symmetry. The unit cell contains 2 Lu, 2 S, and 2 Br atoms, with lattice constants a = 3.955 Å, b = 5.274 Å, and c = 8.085 Å. Our optimized lattice parameters (Table 1) agree well with experimental data. To assess the feasibility of exfoliating a monolayer from the bulk structure, we calculated the interlayer binding energy (E_b). The calculated E_b value, 18.8 meV/ Å^2, is comparable to that of graphite (E_b = 20.30 meV/ Å^2),[25] suggesting that the LuSBr monolayer could be potentially exfoliated from its bulk form.

The orthorhombic symmetry is preserved for the LuSBr monolayer (Fig. 1a), with distinct planar lattice parameters of a = 3.95 Å and b = 5.28 Å. The pleated, non-magnetic structure features tetracoordinated Lu atoms in a checkered arrangement. The average bond lengths are 2.693 Å for Lu-S and 2.778 Å for Lu-Br.

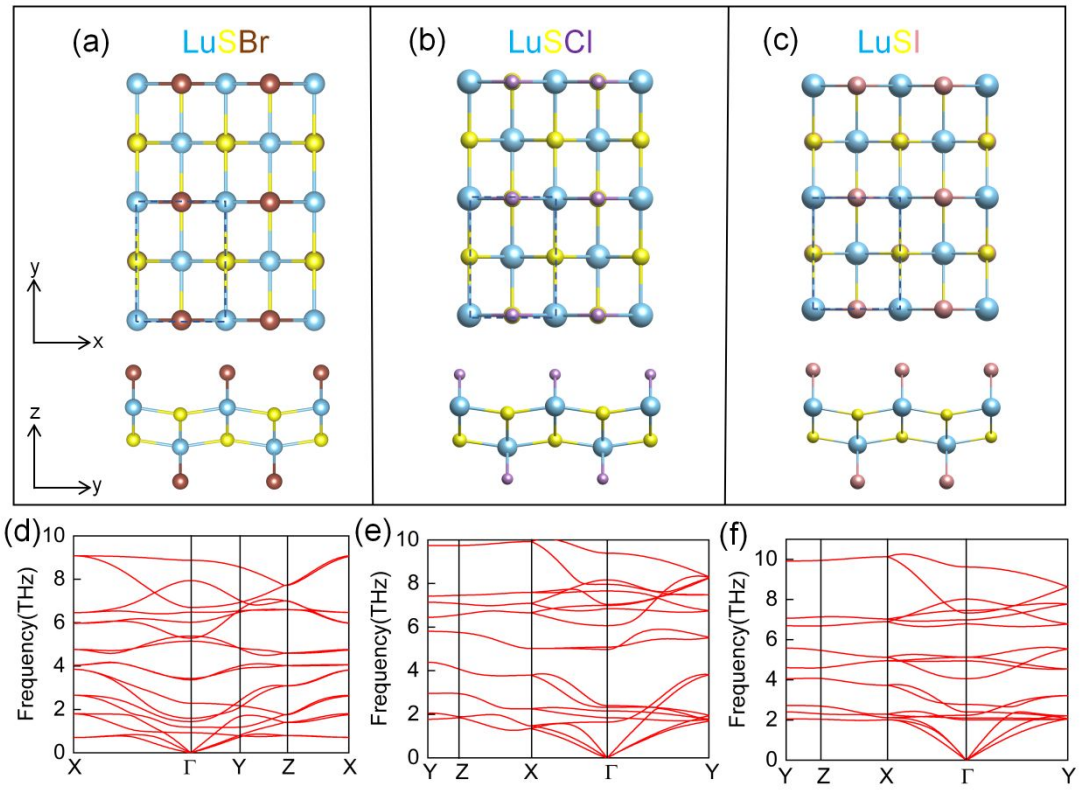

Fig. 1 Top and side views of (a) LuSBr, (b) LuSCl, and (c) LuSI monolayers, along with their corresponding phonon dispersion curves (d-f). The dashed black lines represent the primitive cells.

Substituting Br with Cl or I results in two additional structures: LuSCl and LuSI monolayers (Fig. 1b-1c). The lattice parameters, including lattice constants, space groups, and bond lengths/angles for all three monolayers, are summarized in Table 1. While differences in atomic radii lead to slight variations in bond lengths and lattice constants, these three

monolayers maintain identical structural characteristics. The Bader charge analysis clearly shows that within the three layers, one Lu atom loses approximately 1.8 electrons, while S and X receive about 1.2 and 0.6 electrons, respectively (Table S1).

Table 1. Space group, lattice constants (Å), bond lengths (Å), and angles (°) for LuSX (X= Br, Cl, I) monolayers.

	LuSBr Bulk	**LuSBr layer**	**LuSCl layer**	**LuSI layer**
Space group	Pmmn	Pmmn	Pmmn	Pmmn
Lattice constants	a=3.96, b=5.28 c=9.74	a=3.95 b=5.28	a=3.88 b=5.28	a=4.08 b=5.26
Bond length d_{Lu-S}	2.673	2.693	2.699	2.695
Bond length d_{Lu-X}	2.779	2.778	2.623	3.003
Bond angle (Lu-S-X)	90°	90°	90°	90°

Phonon dispersions were calculated to assess the dynamic stability of LuSX (X=Br, Cl, and I) monolayers (Fig.1d-1f). The absence of soft modes across the entire Brillouin zone confirms the dynamic stability of all three structures. We further evaluated their thermal stability by *ab initio* molecular dynamics (AIMD) simulations at 300 K, 500 K and 800 K. After 5 *ps* simulations (Fig. S1-S2), the structural integrity of three monolayers was well preserved, confirming their high thermal stability.

To ascertain the thermodynamic stability of the monolayers, cohesive energy calculations were performed using the equation:

$$\mathrm{E_{coh}} = [\mathrm{E(LuSX)} - \mathrm{iE}(Lu) - \mathrm{jE(S)} - kE(X)]/(\mathrm{i} + \mathrm{j} + k)$$

where i, j and k indicate the number of atoms, $E(Lu)$, $E(S)$, $E(X)$, and $E(LuSX)$ are the total energies of a single Lu, S, X atom, and one unit cell of the $LuSX$ monolayer, respectively. The calculated cohesive energies of the $LuSBr$, $LuSCl$, and $LuSI$ monolayers are -4.87, -5.08 eV and -4.63 per atom, respectively. These values are comparable to or lower than those of other known monolayers, such as Be–C (-4.82– -4.58 eV per atom)[26-28] and Cu_2Si (-3.46 eV per atom)[29], indicating that these structures are highly stable and form robustly bonded networks.

Furthermore, we evaluated the mechanical stability of LuSX (X=Br, Cl, and I) monolayers by calculating the elastic constants C_{ij}, using the Born's elastic stability criterion. [30] For 2D orthorhombic structures, the criteria require that: $C_{11}, C_{44} > 0$ and $C_{11} + C_{22} - 2C_{12} > 0$. Our results confirm that the LuSX monolayers satisfy these conditions (Table S2), verifying their mechanical stability. As the LuSX monolayers possess high stabilities, one potential method for synthesizing the LuSX monolayer is chemical vapor deposition (CVD).[31] Taking LuSCl as an example, Lu_2S_3 can be used as the precursor for Lu and S, and $LuCl_3$ can be used as the precursor for Lu and Cl, facilitating the synthesis of LuSCl through the reaction $Lu_2S_3 + LuCl_3 \rightarrow 3LuSCl$.

To better understand the structural stability of these LuSX monolayers, we calculated their electron localization functions (ELF). The ELF isosurfaces, observed at a high value of ~0.9 au, are mainly localized around the S atoms and the X atoms (Fig. S3), indicating significant electron localization around these non-metal atoms. Furthermore, the lack of notable ELF between the Lu atoms and the surrounding atoms suggests predominantly ionic bonding. The consistent electron localization patterns across the three different monolayers indicate their similar electronic structures and bonding characteristics.

3.2. Electronic properties

We first calculated the band structures of the LuSX (X= Cl, Br, I) monolayers to explore their electronic properties. As shown in Fig. 2a-2c, all three monolayers exhibit direct-gap semiconducting behavior, with both the conduction band minimum (CBM) and valence band maximum (VBM) located at the Γ point. At the PBE level, the band gaps for LuSBr, LuSCl, and LuSI are 2.92 eV, 2.95 eV, and 2.66 eV, respectively. When using the more advanced hybrid density functional (HSE06), the direct-gap nature is maintained, and the band gaps increase to 4.04 eV, 4.09 eV, and 3.69 eV, respectively. Note that these band gaps are larger than those of many other 2D materials, such as transition metal dichalcogenides (TMDCs), black phosphorus, and CrI_3.[32]

To further explore these monolayers' electronic properties and potential applications, we examined their density of states (DOS) (Fig. 2d-2f). For LuSBr and LuSCl, the VBM is primarily composed of the *p* orbital of S atoms (S-*p*), while the CBM is dominated by the Lu-*d* orbitals. Differently, for LuSI, the VBM is a hybrid dominated by S-*p* and I-*p* orbitals, indicating a more complex electronic structure, while its CBM is mainly composed of the Lu-*d* orbital.

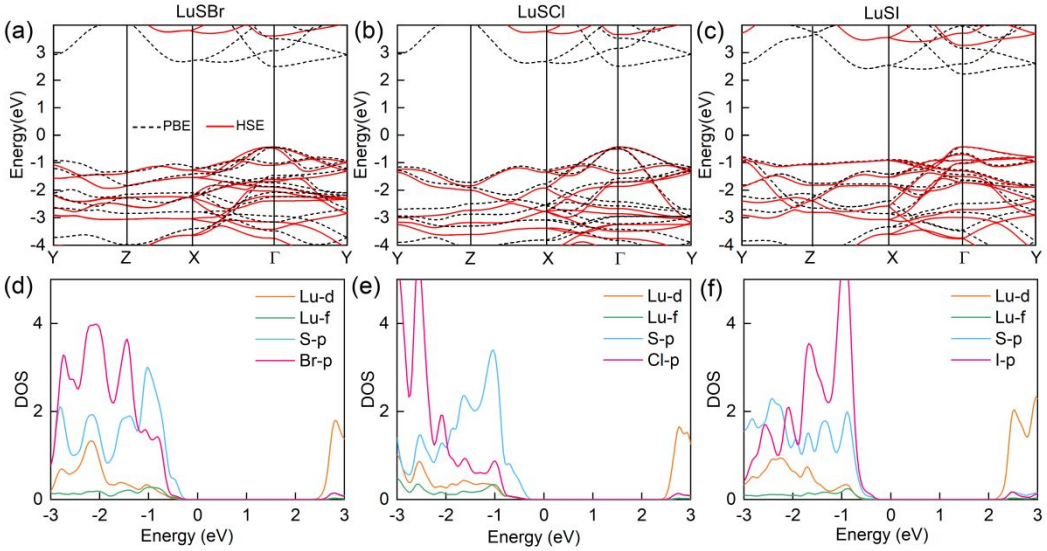

Fig. 2 (a-c) Band structures of the LuSX monolayers calculated by the PBE and HSE06 functionals. (d-f) Density of states for the three monolayers calculated using the PBE functional.

3.3. Electronic structure tunning by external strains

As polarized materials, LuSX monolayers exhibit significant potential for tuning electronic properties through strain, making them promising candidates for flexible electronics and mechanical devices. Typically, strain disturbs the structures' equilibrium state, increasing the systems' total energy. To determine the elastic limits of the LuSX monolayers, we examined their strain-stress relationship under uniaxial strain (Fig. S4). The LuSBr monolayer can withstand a stress up to 6.5 N/m with an ideal strain of 20% along the *y*-direction. Along the *x*-direction, though its ultimate stress is lower (3.2 N/m), the breaking strain increases to 26%. LuSCl and LuSI exhibit slightly lower ultimate stresses (2.4 – 6.0 N/m) and breaking strains (11% - 25 %), yet these values are still higher than those reported for many other 2D materials.[33-35]

We also investigated the effects of biaxial strains (ε, -5% ~ 5%) on the band gaps of the LuSX monolayers (Fig. S5-S6). Across all three monolayers, the direct band gap nature is

preserved, with the band gap (E_g) increasing under tensile strain and decreasing under compressive strain. To quantify the sensitivity of strain on E_g, we calculated the rate of change of E_g ($R(E_g)$) with respect to ε, which is defined as the ratio of the change in band gap to the change in strain, $\Delta E_g/\Delta\varepsilon$. The results show that the absolute values of $R(E_g)$ reach 71 meV/% for LuSBr, 80 meV/% for LuSCl, and 65 meV/% for LuSI, surpassing those observed in single-layer transition metal dichalcogenides, such as MoS_2 (45 meV/%)[36] and $MoSe_2$ (27 meV/%).[37] The pronounced rate of change highlights the high sensitivity of the electronic properties of LuSX monolayers to strain engineering, making them highly promising candidates for strain-sensitive devices. Additionally, the variation of band gaps under uniaxial strain was also presented in Fig. S7, which generally show similar trends compared with that using the biaxial strains.

3.4. Carrier mobilities

To investigate the transport properties of LuSX monolayers, we estimated their carrier mobilities at room temperature using Deformation Potentials (DP) theory by the following expression:[38]

$$\mu_{2D} = \frac{2e\hbar^3 C_{2D}}{3k_B T|m^*|^2 E_d^2}$$

Here e, $\hbar$, K_B and T are the electron charge, reduced Planck constant, Boltzmann constant, and the temperature (set to be 300 K), respectively. Parameter m* represents the effective mass in the transport direction. In-plane stiffness (C_{2D}) is defined as $[\partial^2 E/\partial\delta^2]/S_0$, where E and S_0 denote the total energy and the area of the optimized supercell, respectively. The deformation potential (E_d) is determined as $dE_{edge}/d\varepsilon$, by fitting a linear relation of the band edges (E_{edge}) and applied uniaxial strains (ε).

By applying the above expression, we obtained the carrier mobilities of the LuSX monolayers along different directions. As shown in Table 2, these mobilities are highly anisotropic. Notably, the electron mobility of LuSBr in the *y*-direction (μ_y) reaches 3.18 × 10^3 cm^2 V^{-1} S^{-1}, which is an order of magnitude higher than its mobility in the *x*-direction (0.45×10^3 cm^2 V^{-1} S^{-1}). This value for μ_y in LuSBr surpasses those of 2D transition metal dichalcogenides such as MoS_2 (~10^2 $cm^2 \cdot s^{-1} \cdot V^{-1}$),[39] thus highlighting its superior carrier conductivity.

Table 2. In-plane stiffness C_{2D} (in N/m), effective mass m*, deformation potential E_d, and carrier mobility μ (×10^3 $cm^2 \cdot s^{-1} \cdot V^{-1}$) of LuSBr, LuSCl, and LuSI monolayers along *x*- and *y*-directions.

Phase	Carrier type	$\lvert m_x^*\rvert/m_0$	$\lvert m_y^*\rvert/m_0$	$\lvert E_{1x}\rvert$	$\lvert E_{1y}\rvert$	C_{2Dx}	C_{2Dy}	μ_x	μ_y
LuSBr	electron	1.227	0.178	1.3	3.92	31.04	42.44	0.45	3.18
	hole	0.879	0.27	4.5	3.23			0.074	2.03
LuSCl	electron	0.603	0.42	3.7	2.81	32.18	44.53	0.23	1.18
	hole	1.871	2.775	1.00	3.99			0.34	0.014
LuSI	electron	1.69	8.53	2.4	0.64	29.12	41.61	0.75	0.05
	hole	3.86	4.58	6.3	1.3			0.002	0.04

3.5. Mechanical properties

Building on the strain sensitivity of the electronic properties, we estimated the mechanical properties of the LuSX monolayers, which are crucial for their potential use in flexible devices. We calculated the Young's modulus $Y_{2D}(\theta)$ and Poisson's ratio ν(θ), both of which are highly dependent on the angle of in-plane tensile strain. These values are determined by the following formulas:

$$Y_{2D}(\theta) = \frac{C_{11}C_{22} - C_{12}^2}{C_{11}A^4 + C_{22}B^4 - A^2B^2(2C_{12} - D)}$$
$$\nu(\theta) = \frac{C_{12}(A^4 + B^4) - A^2B^2(C_{11} + C_{22} - D)}{C_{11}A^4 + C_{22}B^4 - A^2B^2(2C_{12} - D)}$$

where $A = \sin\theta$, $B = \cos\theta$, and $D = (C_{11}C_{22} - C_{12}^2)/C_{66}$. Here, θ is the angle between the *x* axis and the direction of in-plane tensile strain.

As shown in Figure 3, the Young's modulus $Y_{2D}(\theta)$ of the LuSX monolayers exhibit significant anisotropy, with maximum values reaching 29.8, 36.1, and 44.2 N/m for LuSBr, LuSCl and LuSI, respectively. These values are comparable to those of phosphorene, which ranges between 23.0 and 92.3 N/m[40]. Additionally, the Poisson's ratios are all positive, with values of 0.24, 0.48, and 0.52, similar to that of FeB_2 monolayer.[41] These results indicate that the LuSX monolayers are relatively soft materials, making them suitable for applications in flexible nanodevices.

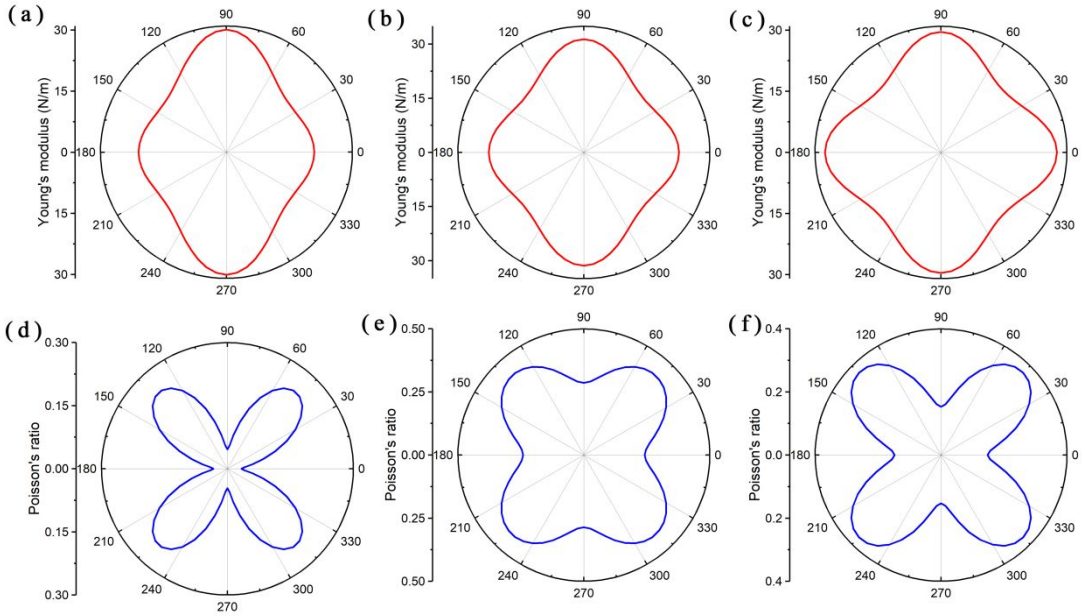

Fig. 3 (a-c) Young's modulus Y_{2D} and (d-f) Poisson ratio ν for LuSBr, LuSCl and LuSI monolayer as a function of the angle.

3.6. Ferroelastic transitions

Ferroelastic (FE) materials are characterized by having two or more equally stable orientation variants that can be switched from one to another without diffusion simply by applying external strains. In the case of LuSX monolayers, two equivalent ground states with identical energy, denoted as the initial state F and the final state F', are illustrated in Fig. 4a-4c. In the initial state F, the lattice condition is $a > b$, in which b is the shorter lattice. Applying uniaxial tensile stress along the x-direction induces a paraelastic state P with $a = b$, which transitions to the final state F', characterized by $a < b$, with the short lattice now oriented along the x-direction. The F' state is effectively a 90° rotation of the F state. Moreover, applying tensile stress in the y-direction to the F' state can revert it to the F state.

For the paraelastic state P, the lattice constants are $a = b = 4.625$ Å for LuSBr, $a = b = 4.580$ Å for LuSCl, and $a = b = 4.685$ Å for LuSI. However, the P states are only metastable and will undergo spontaneous lattice relaxation to the ground state F or F'.

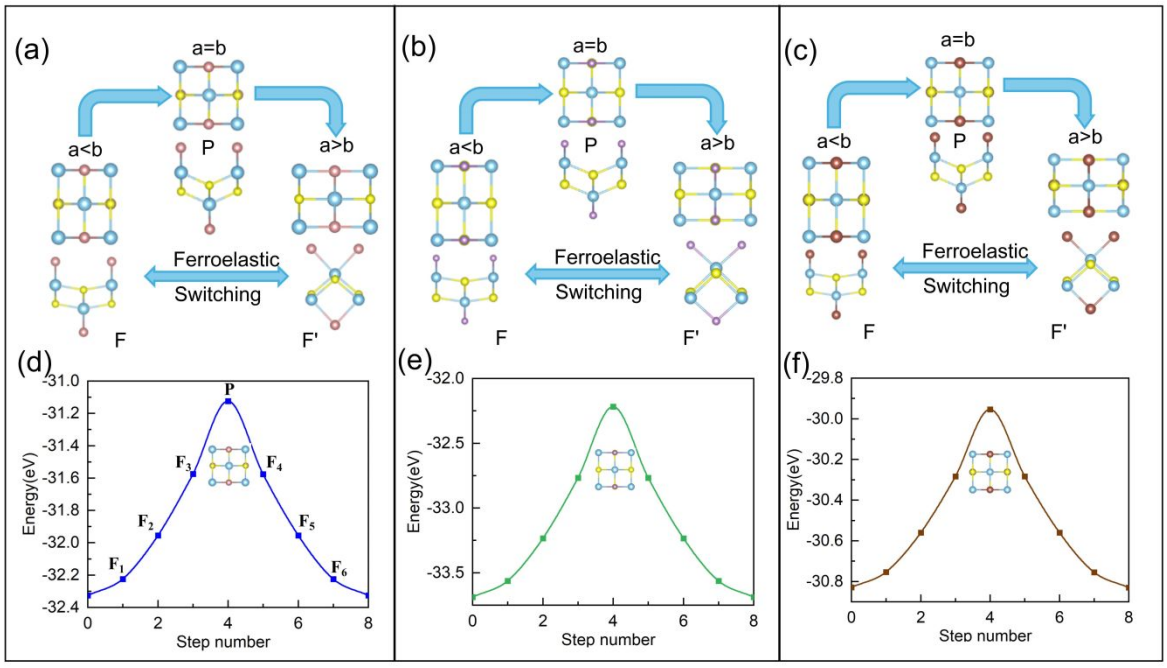

Fig. 4 (a-c) Pathway of FE transition for LuSBr, LuSCl, and LuSI. (d-f) Energy barriers of FE switching for the three monolayers as a function of step number calculated by the nudged elastic band (NEB) method. The intermediate states during FE switching are marked from F_1 to F_6 in (d).

To gain deeper insights into the fundamental physical properties of FE switches, we calculated the transition paths and activation energy barriers using the nudged elastic band (NEB) method.[42, 43] Figure 4d-4f illustrates the energy barriers for FE switching as a function of the step number, indicating that the reaction paths from the F state to the P state and from P to F's state are identical. As expected, the transition state between F and F' is the highly symmetric paraelastic state P, which consistently represents the peak energy point. The overall activation barriers for LuSBr, LuSCl, and LuSI are 0.19 eV, 0.30 eV, and 0.12 eV per atom, respectively. When compared to other 2D FE materials, the FE switching barriers for LuSBr and LuSI are lower than that for BP_5 (0.32 eV per atom),[44] but comparable to those in phosphorene (0.20 eV per atom),[45] and ZrPI monolayer (0.13 eV per atom).[46] These relatively low activation barriers highlight the efficiency of FE switching in LuSX monolayers, beneficial to their applications in nanoscale mechanical and electronic devices.

Reversible FE strain is a key metric for assessing the performance of FE materials. The FE strain is defined as $\left[(|b|/|a| - 1) \times 100\%\right]$. The calculated FE values are 30.4% for LuSBr, 30.9% for LuSCl, and 29.2% for LuSI. These values significantly exceed those of SnS (4.9%) and GeSe (17.8%),[45] and MoSSe (4.7%),[47] and are comparable to phosphorene

(37.9%).[45] This comparison underscores the superior ferroelastic capabilities of LuSX monolayers, highlighting their potential in applications requiring high strain adaptability.

The FE transition between different variants can be quantified using the transformation strain matrix η, which is derived from the Green-Lagrange strain tensor.[48] The transformation strain matrix is expressed as $\eta_y = \left(\left[H_{ref}^{-1}\right]^T H_y^T H_y H_{ref}^{-1} - I\right)/2$, where *I* is a 2 × 2 identity matrix, and H_y and H_{ref} represent the lattice constants of the FE and paraelastic states along the *x*- and *y*-directions, respectively. For LuSBr, LuSCl, and LuSI, the lattice constants H_y are [3.95,0;0,5.28], [3.88,0;0,5.28], and [4.08,0;0,5.26], respectively, with H_{ref} being [4.625,0;0,4.625], [4.580,0;0,4.580], [4.685,0;0,4.685], respectively. Based on these values, the calculated strain matrix η_y for the initial variant F is [-0.136,0;0,0.151], [-0.142,0;0,0.163], and [-0.122,0;0,0.129] for LuSBr LuSCl, and LuSI, respectively. These values correspond to compressive strains of 13.6%, 14.2%, and 12.2% in the *x*-direction and tensile strains of 15.1%, 16.3%, and 12.9% in the *y*-direction, respectively. Similarly, the diagonal matrix η_x for the final variant F' for LuSBr, LuSCl, and LuSI yields [0.151,0;0,-0.136], [0.163,0;0,-0.142] and [0.129,0;0,-0.122], indicating tensile strains of 15.1%,16.3%, and 12.9% in the *x*-direction and compressive strains of 13.6%, 16.3%, and 12.2% in the *y*-direction, respectively. Obviously, the ferroelasticity of these LuSX monolayers significantly surpasses those of other 2D materials, such as SnS (1.9% along *x* and 2.8 % along *y*) and GeSe (2.7% along *x* and 4.1 % along *y*)[49].

The above analyses clearly show that LuSX monolayers are intrinsic FE materials, enabling control of direction-dependent electronic behaviors through ferroelastic switching. Taking LuSBr as an example, its F' phase possesses high electron mobility along the *x* direction

(3.18×10^3 cm^2 V^{-1} S^{-1}) and low mobility along the *y*-direction (0.45×10^3 cm^2 V^{-1} S^{-1}), which is the opposite of the F phase. Consequently, the direction of electric conductance can be switched between the *x* and *y* directions *via* FE switching, which would facilitate charge separation and migration during photocatalytic reactions.

3.7. Photocatalytic water splitting

For a 2D semiconductor to be a viable candidate for photocatalytic water splitting, it must meet several key criteria. Firstly, the semiconductor's band gap should exceed 1.23 eV to drive hydrogen and oxygen evolution reactions. Secondly, photogenerated carriers must be quickly transferred to prevent electron-hole recombination at the surface. For example, the distinctive FE switching capability of the LuSBr monolayer could enable controlled directionality of electron and hole mobility, which might spatially separate them, thereby reducing recombination rates and enhancing photocatalytic efficiency. Thirdly, the band structure must be appropriately aligned with the redox potentials of water: the CBM should be higher than the reduction potential of H^+/H_2 (-4.44 eV), and the VBM must be lower than the oxidation potential of O_2/H_2O (-5.67 eV). Taking into account the impact of pH, the reduction potential of H^+/H_2 ($E^{red}(H^+/H_2)$) and the oxidation potential of H_2O/O_2 ($E^{ox}(H_2O/O_2)$) can be expressed as $E^{red}(H^+/H_2) = -4.44 + pH\times0.059$ eV and $E^{ox}(H_2O/O_2) = -5.67 + pH\times0.059$ eV, respectively.[50, 51] Proper alignment ensures efficient and feasible charge transfer for the redox processes involved in water splitting.[52]

Since LuSX monolayers meet the band gap requirement, we next evaluated their band edge alignment relative to the vacuum energy level. As the F' phase is symmetry-related with F phase, but show different shape of the Brillouin Zone, we also presented the band structures

for the F' phase (Fig. S8) in the ESI. As depicted in Figure 5, at pH = 0, the CBM positions for the F, F', and P phases of LuSBr are -3.44 eV, -3.44 eV, and -3.18 eV respectively, all of which lie above the hydrogen reduction potential. Similarly, their VBM positions are -7.49 eV, -7.49 eV, and -6.67 eV respectively, all below the water oxidation potential. This alignment satisfies the thermodynamic prerequisites for full water splitting. A similar trend was observed in the LuSCl and LuSI monolayers, where the band alignments effectively bridge the redox potentials of water, indicating their suitability for photocatalytic water-splitting applications. Notably, in neutral (pH=7) and alkaline (pH=14) conditions, all three layers maintain favorable band alignments, indicating their capability to catalyze water splitting across a range of pH levels.[53]

To further evaluate the photocatalytic potential of LuSX monolayers, we calculated the photo-generated electron and hole potentials for water splitting under different pH conditions, using the LuSBr monolayer as an example. At pH=0, the potential of photo-generated electrons for the hydrogen reduction reaction (U_e), defined as the energy difference between the hydrogen reduction potential and the CBM, is at 1.0 eV; The potential of photo-generated holes for water oxidation (U_h), defined as the energy difference between the VBM and the oxidation potential, is at 1.82 eV. At pH = 7 the U_e and U_h values are 0.587 and 2.223 V, respectively. These values suggest active photocatalytic activity of the LuSBr monolayer in both acidic and neutral environments.[54] Furthermore, the U_e and U_h values remain consistent in the F and F' phases of LuSBr, but differ in the P phase. This variation indicates that U_e and U_h can be significantly modulated during the FE switching process. Similar trends are observed in LuSCl and LuSI monolayers, as indicated by the pH-dependent photo-generated electron and hole potentials provided in Table S3.

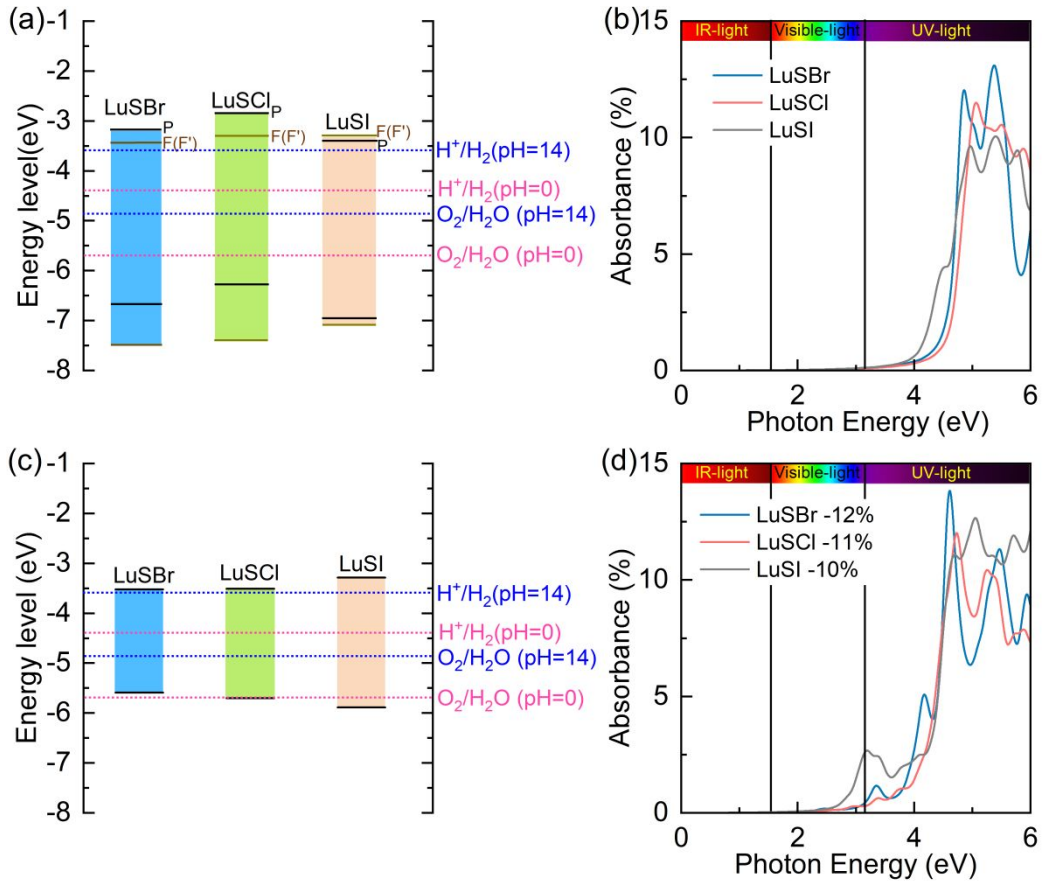

Fig. 5 (a) Band-edge positions of strain-free LuSBr, LuSCl, and LuSI monolayers relative to the redox potentials of water calculated using the HSE06 functional. The band edges of F, P, and F' phases are marked by different lines. The vacuum energy level is set to 0 eV. (b) Light absorbance spectra of the three monolayers calculated using the HSE06 functional. (c-d) Band-edge positions and light absorbance for the same monolayers under applied strains of -12% (LuSBr), -11% (LuSCl), and -10% (LuSI).

An efficient photocatalyst should be able to harvest solar light efficiently. We therefore plotted the light absorbance spectra for the three LuSX monolayers (Figure 5b). All three layers display strong absorption in the ultraviolet (UV) region (> 4 eV), suggesting their potential as efficient UV-driven photocatalysts,[55] similar to the widely studied titanium-based photocatalysts such as TiO_2.[1] Among the three, LuSI shows slightly stronger absorption at

higher energy levels, indicating superior UV performance. Overall, their strong UV absorption and favorable band edge alignments make these monolayers promising candidates for photocatalytic water splitting under UV light.

However, since UV light represents only a small portion of the solar spectrum, strategies such as doping, heterostructuring, or strain engineering could be explored to extend their absorption into the visible range for better solar efficiency. The optimal band gap for a photocatalyst to achieve the best performance for water splitting is typically in the range of 1.8 to 2.2 eV.[56] To explore this, we first applied compressive strain to LuSCl as a test case, successfully tuning its band gap to 2.19 eV with a strain of -11 %(Fig. S9b). A similar trend is observed in LuSBr, where a -12% strain reduces the band gap to 2.07 eV (Fig. S9a). For LuSI, though it fractures at -11% strain, a reduced band gap of 2.6 eV can be achieved at -10% strain (Fig. S9c). While this value remains outside the optimal range for water splitting, it still represents an improvement over the strain-free structure. Notably, experimental studies have already demonstrated strains exceeding 10%[57]. Furthermore, both LuSCl at -11% strain and LuSI at -10% strain maintain favorable band alignments for water splitting across all pH levels (Fig. 5c). However, LuSBr, while not suitable at pH = 0, remains active for water splitting when the pH is greater than 2.

Furthermore, in all three strained monolayers, there is a noticeable red shift in the absorption edges within the light absorption spectrum (Fig. 5d), making them more responsive to visible light. Thus, strain engineering not only effectively modulates the band gaps but also enhances the materials' light absorption in the visible range. As a result, these stained monolayers maintain favorable band alignments for water splitting while simultaneously

improving their ability to harvest visible light, which is crucial for developing efficient photocatalysts.

Finally, we investigated how FE switching directly impacts the overall efficiency of water splitting. In Figure S10-S12, we present the shifts in band edge positions across various intermediate states (ranging from F_1 to F_6) during FE switching. For LuSBr, it is evident that at pH=0, during the transition from the F state to the P state, the potential of photo-generated electrons for the hydrogen reduction reaction (U_e) gradually increases from 1.0 eV to 1.27 eV, while the potential of photo-generated holes for water oxidation (U_h) decreases from 1.82 eV to 1.0 eV. In the P state, U_e and U_h achieve a more balanced potential compared to the F state. A similar pattern is found during the transition from the F' to P states.

Conversely, the LuSI sheet displays a different trend. The potential U_e initially increases from the F state to the F_3 state and then slightly decreases to the P state, whereas the potential U_h follows a similar pattern but drops earlier at the F_2 state. This analysis clearly demonstrates that FE switching significantly impacts the potential for both hydrogen reduction and water oxidation, thereby influencing the overall efficiency of water splitting.

4. Conclusions

In this work, we demonstrated that the LuSX (X=Cl, Br, I) monolayers represent a novel family of FE materials with remarkable potential for photocatalytic water splitting. A key characteristic of these materials is the strain-driven 90° lattice rotation during the FE phase transition with low switching barriers estimated at 0.19 eV, 0.30 eV, and 0.12 eV/atom for LuSBr, LuSCl, and LuSI, respectively. The corresponding reversible FE strains are 30.4%, 30.9%, and 29.2%, contributing to their excellent FE performance.

Furthermore, our study revealed that all three monolayers are highly suitable for photocatalytic water splitting. Through strain engineering, the band gaps of LuSX monolayers can be tuned to achieve values within the optimal range for water splitting. Notably, LuSCl and LuSI monolayers, under stains of -11% and -10%, respectively, maintained suitable band alignment across all pH values for water splitting. For LuSBr, when subjected to a strain of 12%, it becomes suitable for water splitting at pH levels exceeding 2. In addition, these strained monolayers can better harvest visible light, thus improving their photocatalytic efficiency.

This unique combination of excellent ferroelastic behavior, low switching barriers, and strong photocatalytic performance in the LuSX monolayers offers a significant opportunity to advance the application of FE materials in energy-related fields, particularly in photocatalytic water splitting. This work paves the way for innovative explorations of FE materials, potentially inspiring researchers to further expand the use of FE materials in broader energy applications such as electrocatalysts or batteries, thereby meeting the growing demand for sustainable energy solutions.

Acknowledgments

This work is supported in China by the National Natural Science Foundation of China (Grant No. 12204144), the Natural Science Foundation of Hebei Province (Grant No. A2022205027, and A2024205029), financial support program from Hebei Province (Grant No. C20220503, and C20230509), and in USA by the Department of Energy (Grant DE-SC0023418).

References

1. A. Fujishima and K. Honda, *Nature*, 1972, **238**, 37-38.

2. C. A. Hall, P. Ferrer, D. C. Grinter, S. Kumar, I. da Silva, J. Rubio-Zuazo, P. Bencok, F. de Groot, G. Held and R. Grau-Crespo, *J. Mater. Chem. A*, 2024, **12**, 29645-29656.

3. Y. Zhao, S. Zhang, R. Shi, G. I. N. Waterhouse, J. Tang and T. Zhang, *Mater. Today*, 2020, **34**, 78-91.

4. W. Yang, X. Zhang and Y. Xie, *Nano Today*, 2016, **11**, 793-816.

5. Q.-W. He, J.-H. Wang, D.-Y. Zhu, D.-S. Tang, Z. Lv, F. Guo and X.-C. Wang, *Nano Lett.*, 2024, **24**, 8979-8987.

6. Z. Gao, F. Ma, H. Wu, Y. Ge, Z. Zhu, Y. Liu, Y. Jiao and Z. Chen, *J. Mater. Chem. A*, 2023, **11**, 3717-3724.

7. Y. Zhou, Y. Zhang, M. Lin, J. Long, Z. Zhang, H. Lin, J. C. S. Wu and X. Wang, *Nat. Commun.*, 2015, **6**, 8340.

8. J. Xiong, J. Di, J. Xia, W. Zhu and H. Li, *Adv. Funct. Mater.*, 2018, **28**, 1801983.

9. H. Yu, M. Dai, J. Zhang, W. Chen, Q. Jin, S. Wang and Z. He, *Small*, 2023, **19**, 2205767.

10. Y. Miao, Y. Zhao, S. Zhang, R. Shi and T. Zhang, *Adv. Mater.*, 2022, **34**, 2200868.

11. Y. Li, J. Li, W. Yang and X. Wang, *Nanoscale Horiz.*, 2020, **5**, 1174-1187.

12. M. J. Jacinto, L. F. Ferreira and V. C. Silva, *J. Sol-Gel Sci. Technol.*, 2020, **96**, 1-14.

13. M. Wang, L. Cai, Y. Wang, F. Zhou, K. Xu, X. Tao and Y. Chai, *J. Am. Chem. Soc.*, 2017, **139**, 4144-4151.

14. K. Aizu, *J. Phys. Soc. Jpn*, 1969, **27**, 387-396.

15. P. Man, L. Huang, J. Zhao and T. H. Ly, *Chem. Rev.*, 2023, **123**, 10990-11046.

16. E. K. H. Salje, *Annu. Rev. Mater. Res.*, 2012, **42**, 265-283.

17. C. Xu, J. Mao, X. Guo, S. Yan, Y. Chen, T. W. Lo, C. Chen, D. Lei, X. Luo, J. Hao, C. Zheng

and Y. Zhu, *Nat. Commun.*, 2021, **12**, 3665.

18. J.-H. Yuan, G.-Q. Mao, K.-H. Xue, J. Wang and X.-S. Miao, *Nanoscale*, 2020, **12**, 14150-14159.

19. X. Ding, Y. Jia and G. Gou, *J. Phys. Chem. Lett.*, 2023, **14**, 420-429.

20. X. Liu, L. Li, C. Yang, C. Bai and J. Li, *J. Mater. Chem. A*, 2023, **11**, 21735-21745.

21. G. Kresse and J. Furthmüller, *Phys. Rev. B*, 1996, **54**, 11169-11186.

22. P. E. Blöchl, *Phys. Rev. B*, 1994, **50**, 17953.

23. J. P. Perdew, K. Burke and M. Ernzerhof, *Phys. Rev. Lett.*, 1996, **77**, 3865-3868.

24. S. Baroni, S. de Gironcoli, A. Dal Corso and P. Giannozzi, *Rev. Mod. Phys.*, 2001, **73**, 515-562.

25. H. Peng, Z.-H. Yang, J. P. Perdew and J. Sun, *Phys. Rev. X*, 2016, **6**, 041005.

26. C.-S. Liu, H.-H. Zhu, X.-J. Ye and X.-H. Yan, *Nanoscale*, 2017, **9**, 5854-5858.

27. Y. Wang, F. Li, Y. Li and Z. Chen, *Nat. Commun.*, 2016, **7**, 11488.

28. B. Wang, S. Yuan, Y. Li, L. Shi and J. Wang, *Nanoscale*, 2017, **9**, 5577-5582.

29. L.-M. Yang, V. Bačić, I. A. Popov, A. I. Boldyrev, T. Heine, T. Frauenheim and E. Ganz, *J. Am. Chem. Soc.*, 2015, **137**, 2757-2762.

30. F. Mouhat and F.-X. Coudert, *Phys. Rev. B*, 2014, **90**, 224104.

31. Y. Tang, Y. Ping, X. Yang, J. Xing, J. Chen, X. Wang, J. Lu, H. Jing, K. Liu, J. Wu, X. Zhou, T. Zhai and H. Xu, *Adv. Mater.*, **n/a**, 2405358.

32. A. Chaves, J. G. Azadani, H. Alsalman, D. R. da Costa, R. Frisenda, A. J. Chaves, S. H. Song, Y. D. Kim, D. He, J. Zhou, A. Castellanos-Gomez, F. M. Peeters, Z. Liu, C. L. Hinkle, S.-H. Oh, P. D. Ye, S. J. Koester, Y. H. Lee, P. Avouris, X. Wang and T. Low, *npj 2D Mater. Appl.*, 2020, **4**, 29.

33. F. Ma, Y. Jiao, W. Wu, Y. Liu, S. A. Yang and T. Heine, *Nano Lett.*, 2021, **21**, 2356-2362.

34. Y. Jiao, F. Ma, G. Gao, J. Bell, T. Frauenheim and A. Du, *J. Phys. Chem. Lett.*, 2015, **6**, 2682-2687.

35. T. Li, *Phys. Rev. B*, 2012, **85**, 235407.

36. H. J. Conley, B. Wang, J. I. Ziegler, R. F. Haglund, Jr., S. T. Pantelides and K. I. Bolotin, *Nano Lett.*, 2013, **13**, 3626-3630.

37. J. O. Island, A. Kuc, E. H. Diependaal, R. Bratschitsch, H. S. J. van der Zant, T. Heine and A. Castellanos-Gomez, *Nanoscale*, 2016, **8**, 2589-2593.

38. J. Bardeen and W. Shockley, *Physical Review*, 1950, **80**, 72-80.

39. A. Rawat, N. Jena, Dimple and A. De Sarkar, *J. Mater. Chem. A*, 2018, **6**, 8693-8704.

40. L. Wang, A. Kutana, X. Zou and B. I. Yakobson, *Nanoscale*, 2015, **7**, 9746-9751.

41. C. Zhang, T. He, S. K. Matta, T. Liao, L. Kou, Z. Chen and A. Du, *J. Phys. Chem. Lett*, 2019, **10**, 2567-2573.

42. G. Mills, H. Jónsson and G. K. Schenter, *Surf. Sci.*, 1995, **324**, 305-337.

43. H. JÓNSSON, G. MILLS and K. W. JACOBSEN, in *Classical and Quantum Dynamics in Condensed Phase Simulations*, 1998, DOI: 10.1142/9789812839664_0016, pp. 385-404.

44. H. Wang, X. Li, J. Sun, Z. Liu and J. Yang, *2D Mater.*, 2017, **4**, 045020.

45. M. Wu and X. C. Zeng, *Nano Lett.*, 2016, **16**, 3236-3241.

46. T. Zhang, Y. Ma, L. Yu, B. Huang and Y. Dai, *Mater. Horiz.*, 2019, **6**, 1930-1937.

47. Y. Ma, L. Kou, B. Huang, Y. Dai and T. Heine, *Phys. Rev. B*, 2018, **98**, 085420.

48. W. Li and J. Li, *Nat Commun*, 2016, **7**, 10843.

49. S.-H. Zhang and B.-G. Liu, *Nanoscale*, 2018, **10**, 5990-5996.

50. X. Lv, L. Yu, F. Li, J. Gong, Y. He and Z. Chen, *J. Mater. Chem. A*, 2021, **9**, 6993-7004.

51. Y. Liu, W. Li, F. Li and Z. Chen, *J. Mater. Chem. A*, 2023, **11**, 20254-20269.

52. Y. Li, Y.-L. Li, C. M. Araujo, W. Luo and R. Ahuja, *Catal. Sci. Technol.*, 2013, **3**, 2214-2220.

53. M. Qiao, J. Liu, Y. Wang, Y. Li and Z. Chen, *J. Am. Chem. Soc.*, 2018, **140**, 12256-12262.

54. S. Chen and L.-W. Wang, *Chem. Mater.*, 2012, **24**, 3659-3666.

55. R. Li and C. Li, in *Advances in Catalysis*, ed. C. Song, Academic Press, 2017, vol. 60, pp. 1-57.

56. T. Nano LettersLe Bahers, M. Rérat and P. Sautet, *J. Phys. Chem. C*, 2014, **118**, 5997-6008.

57. K. S. Kim, Y. Zhao, H. Jang, S. Y. Lee, J. M. Kim, K. S. Kim, J.-H. Ahn, P. Kim, J.-Y. Choi and B. H. Hong, *Nature*, 2009, **457**, 706-710.

The data that support the findings of this study are included within the article.